# Cryo-Balloon Catheter Localization Based on a Support-Vector-Machine Approach

Tanja Kurzendorfer, Philip W. Mewes, Andreas Maier, Norbert Strobel, and Alexander Brost

***Abstract*—Cryo-balloon catheters have attracted an increasing amount of interest in the medical community as they can reduce patient risk during left atrial pulmonary vein ablation procedures. As cryo-balloon catheters are not equipped with electrodes, they cannot be localized automatically by electro-anatomical mapping systems. As a consequence, X-ray fluoroscopy has remained an important means for guidance during the procedure. Most recently, image guidance methods for fluoroscopy-based procedures have been proposed, but they provide only limited support for cryo-balloon catheters and require significant user interaction. To improve this situation, we propose a novel method for automatic cryo-balloon catheter detection in fluoroscopic images by detecting the cryo-balloon catheter's built-in X-ray marker. Our approach is based on a blob detection algorithm to find possible X-ray marker candidates. Several of these candidates are then excluded using prior knowledge. For the remaining candidates, several catheter specific features are introduced. They are processed using a machine learning approach to arrive at the final X-ray marker position. Our method was evaluated on 75 biplane fluoroscopy images from 40 patients, from two sites, acquired with a biplane angiography system. The method yielded a success rate of 99.0 % in plane A and 90.6 % in plane B, respectively. The detection achieved an accuracy of 1.00 mm $\pm$ 0.82 mm in plane A and 1.13 mm $\pm$ 0.24 mm in plane B. The localization in 3-D was associated with an average error of 0.36 mm $\pm$ 0.86 mm.**

***Index Terms*—Ablation, Atrial Fibrillation, Cryo-Balloon, Detection, Electrophysiology, Fluoroscopy, Left Atrium.**

## I. Introduction

PHARMACOTHERAPY is often used to prevent atrial fibrillation. However, this therapy may fail if drugs are not taken as prescribed, and it may be costly for younger patients. Therefore, minimally invasive catheter ablation had been proposed as an alternative treatment option for atrial fibrillation, in particular paroxysmal atrial fibrillation [1], [2], [3]. Moreover, catheter ablation was recently upgraded by the European Society of Cardiology (ESC) to be considered as a first line of treatment [4]. The American Heart Association (AHA) lists catheter ablation for paroxysmal AFib as a *Class 1* treatment option as well [5]. In the past decade, pulmonary vein isolation (PVI) by catheter ablation has proven to be a save and effective approach for dealing with paroxysmal atrial fibrillation [5], [6], [7], [8]. The goal of this procedure is the electrical isolation of the four pulmonary veins (PVs) connected to the left atrium (LA), since triggers causing atrial fibrillation predominantly reside inside the PVs. The catheter ablation procedures are performed in electrophysiology (EP) labs. A standard ablation procedure involves at least a linear radio-frequency (RF) ablation catheter. With this catheter, point-by-point ablation around the ostium of the pulmonary veins is performed to achieve signal block. Risk factors of this approach are - among others - pulmonary vein stenosis and esophageal fistula [6], [9]. To reduce these risks, cryo-balloon catheter ablation techniques can be used [10], [11], [12]. In fact, the most recent guidelines recommend cryo-balloon ablation as an alternative to the point-wise radio-frequency catheter ablation [5]. The success of the cryo-balloon catheter depends on the underlying anatomy of the patient [13]. Cryo-balloon catheters isolate a pulmonary vein by freezing the tissue antrally around its ostium using liquid nitrogen injected into the balloon device [14]. At the time of this writing, two cryo-balloon generation were commercially available, and the third cryo-balloon generation has recently been introduced. The first generation of the cryothermal balloon catheter is shown in Figure 1 (a). Two different balloon sizes were and are still available, either with a diameter of 23 mm or 28 mm. The size of the balloon is chosen to match the underlying patient anatomy. As no Achieve mapping catheter was available together with the first cryo-balloon catheter, a second transseptal puncture was required for a circumferential mapping (lasso) catheter. The lasso catheter measures the electrical signals coming from the PVs. After the ablation with the cryo-balloon catheter, the lasso catheter is placed at a PV ostium to confirm the signal block through PV isolation. As this is time consuming and associated with a second transseptal puncture, the Achieve spiral mapping catheter was introduced together with the second generation of cryo-balloon catheter, see Figure 1 (b) for an example. This catheter set allows for a single transseptal puncture, as the mapping catheter can be inserted through the shaft of the cryothermal balloon catheter into the PV to monitor electrical signals. Furthermore, the second generation of cryo-balloon catheter was found to reduce the procedure time as fewer freezes are required to achieve PVI due to its better cooling properties. Another advantage is that the electrical signal can be measured both during and immediately after the ablation with the mapping catheter inside the PV. The cryo-balloon is a so-called single shot device as it can, at least in principle, achieve PV isolation with only one single application [5]. If the device is used successfully, it promises a reduction of procedure time, X-ray dose and risks for complications [6],

T. Kurzendorfer and A, Maier are with the Pattern Recognition Lab, Friedrich-Alexander-University Erlangen-Nuremberg, Erlangen, Germany, e-mail: tanja.kurzendorfer@fau.de.

P.W. Mewes, N. Strobel, and A. Brost are with Siemens Healthcare GmbH, Advanced Therapies, Forchheim, Germany.

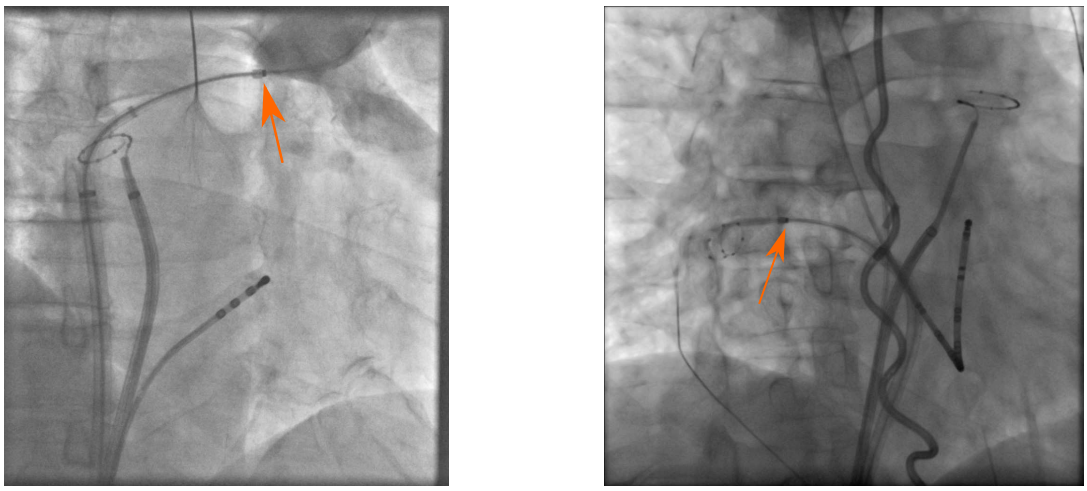

(a) (b)

Fig. 1. (a) Fluoroscopic image showing a first generation cryo-balloon catheter, circumferential mapping catheter and a catheter in the coronary sinus, the so called CS catheter. The orange arrow points to the X-ray marker of the cryo-balloon catheter, which has to be detected. (b) Fluoroscopic image showing a second generation cryothermal balloon catheter, where the lasso catheter has been inserted through the shaft of the cryo-balloon catheter. Furthermore a temperature probe, CS catheter and a lasso catheter are present in the fluoroscopic image. The orange arrow points to the X-ray marker of the cryo-balloon catheter, which has to be detected.

[12], [15], [16]. Since cryo-balloon catheters are not equipped with electrodes or electromagnetic sensors unlike traditional RF ablation catheters, they are invisible to electro-anatomical mapping systems (EAMS). EAMS either are impedance based, or they use an electro-magnetic field to localize catheters in 3-D. Once devices have been localized, they can be visualized with respect to a 3-D representation of the LA. As currently available navigation systems do not provide support for cryo-balloon catheters, the most commonly used navigation tool available to the physician remains X-ray imaging. Trans-esophageal-echo (TEE) is not routinely used during catheter ablation procedures, due to the requirement of general anesthesia. In fact, TEE itself may also contribute to esophageal injury [17]. Intra-cardiac echography (ICE) is another tool to help during catheter positioning, but is most commonly used to guide the transseptal puncture [18]. Recently, ICE has been employed to guide cryo-balloon ablation procedures. However, in the study by Su et al. [18], venograms are still recommended to assess the position of the cryo-balloon catheter. Nevertheless, there are advantages of ICE, such as palpation monitoring and balloon positioning. Unfortunately, the lack of reimbursement of ICE catheters in multiple countries in Europe is limiting its use.

During X-ray procedures, physicians try to keep the X-ray dose to a minimum. As a result, the cryo-balloon catheter may be hard to see under fluoroscopy in certain cases [19]. Therefore, methods to detect and localize the cryothermal balloon catheter are helpful to improve this procedure. A first detection method of cryo-balloon catheters in fluoroscopic images using a simple blob detection was proposed in [20]. However, only the characteristics directly derived from the blob detection were exploited to make a decision about the final catheter position. We used this approach as a starting point for our current method and extended it using a novel image-based feature. In addition, we introduced a kernel-based support-vector-machine (SVM) to implement a classifier that is able to accurately detect the X-ray marker attached to the cryo-balloon catheter, see Fig. 1. To be more precise, the detected balloon marker is a radio-opaque marker attached to the shaft of the cryo-balloon catheter next to the injection-port of the liquid nitrogen, which is located in the first third of the cryo-balloon. As the previous method only supported monoplane C-arm systems, we propose an extension to biplane systems which enables the reconstruction of the cryo-balloon catheter marker in 3-D.

## II. Previous Work

Brost et al. [21], [22], [23] proposed a method for 3-D respiratory motion compensation during electrophysiology procedures using a 3-D lasso-catheter model and a biplane C-arm system. The initialization of the lasso-catheter had to be done manually. Afterwards the lasso catheter was extracted using fast marching, and a 2-D ellipse was fitted to the result for both imaging planes. In the next step, the catheter was reconstructed in 3-D knowing the biplane X-ray projections and considering an elliptical shape of the lasso-catheter. This model was then used for tracking the respiratory motion. A similar work for respiratory motion compensation was proposed by Ma et al. [24]. Here the motion estimate was obtained by localizing an electrode of the coronary sinus (CS) catheter. To detect the catheter electrodes a blob detection method was used. A cost function was applied to distinguish the electrodes of the CS catheter from other catheter electrodes. For the respiratory motion correction, the proximal electrode of the CS catheter was relied on. An extension of the two previous described methods was proposed by Brost et al. [25]. In this work a combined cardiac and respiratory motion compensation algorithm for atrial fibrillation procedures was presented. To this end, a joined approach of the two previous methods was applied. The CS catheter was used as a point of reference, if

larger movements of the circumferential lasso catheters had been detected. For example, when the catheter was moved from one pulmonary vein to another. The motion estimate itself, was still derived from the lasso catheter. However, also this method relied on initial manual catheter localization.

Hoffmann et al. [26] proposed a semi-automatic catheter reconstruction workflow from two views. In this paper three different types of catheters were considered, the radio-frequency ablation catheter, the coronary sinus catheter and the circumferential lasso catheter. The method required a seed-point for the localization of the catheter in the fluoroscopic images. Based on this starting point, a graph searched was initialized to detect the rest of the catheter shaft. In case of biplane images, correspondences were selected and used for the 3-D catheter reconstruction.

Almost all of the presented methods heavily rely on manual user initialization and they have not yet considered a cryothermal balloon catheter. To the best of our knowledge, the first solution for cryo-balloon catheter localization in fluoroscopic images was proposed by Kurzendorfer et al. [20]. The radio-opaque marker of the cryo-balloon catheter was detected using a blob based method in combination with a cost function. This prior work is used as reference to highlight the improvements made with the novel approach presented in this paper.

## III. Methods

Depending on the patient size, the C-arm view angle, and the X-ray dose settings, the cryothermal balloon itself may be hard to see in fluoroscopic images. The X-ray marker attached to the shaft of the cryo-balloon catheter on the other hand can be easier to find. This is why we consider it a good alternative for detecting the cryo-balloon catheter in the fluoroscopic images, in particular when combining detection and improved visualization. Our approach comprises four steps. First, a Hessian blob-detection is performed to detect potential cryo-balloon X-ray marker candidates which have a round shape and are attached to the shaft of the cryo-balloon catheter. Many of them are already excluded by applying standard criteria using prior knowledge. In the second step, additional features are calculated for the remaining marker candidates. In the third step, these features are classified by a SVM and the result of this classification is further processed to arrive at a final position estimate for the A-plane image of a biplane C-arm system, i. e., the right-anterior-oblique (RAO) view using a typical biplane view setup. In the fourth step, the cryo-balloon X-ray marker is detected in the B-plane image , i. e., the left-anterior-oblique (LAO) view using a typical biplane view setup. This can either be achieved by the same three steps or using just the first step and epipolar constraints to find the corresponding marker position in plane B. Once, the 2-D position of the X-ray marker is known in the RAO plane (A plane) and the LAO plane (B plane), the position in 3-D is computed.

### A. Blob Detection

First, the information about the collimators from the DICOM header is used to crop the image. In a real-time set up, such information is readily available from the C-arm system. The image processing steps afterwards are just performed on the region of interest. After the collimator removal we have a cropped image, denoted as $\mathbf{I}(u,v) \in \mathbb{Z}^{N\times M}$ of size $N \times M$. A histogram equalization is carried out to enhance the difference between the cryo-balloon catheter and the surrounding tissue. The histogram equalization is applied to the cropped image only. In the next step, the histogram equalized image is processed with a blob detection algorithm. The blob detector is based on the Hessian matrix [24]. The blob detector is not multi-scale, because the X-ray marker of the cryo-balloon catheter has always the same size, no matter which type of the cryo-balloon catheter is used. For the Hessian matrix the second derivatives of the image $\mathbf{I}(u,v)$ are required. As fluoroscopic images are prone to noise, additional Gaussian smoothing is used. The standard deviation $\sigma$ of the Gaussian filter kernel is matched to the diameter of the X-ray marker from the cryothermal balloon catheter. As the width of the marker is known and the pixel spacing is available, either from DICOM information or C-arm parameters, the standard deviation $\sigma$ of the Gaussian can be adjusted accordingly. During our experiments, we found out, however, that a fixed width is sufficient as long as the device is used within a limited region in 3-D space. For our application, this is a space around the biplane C-arm system's iso-center with a diameter of 30 mm to 40 mm (average size of a left atrium). Smoothing and taking derivatives can be performed in one filtering step by convolving the image with the second derivatives of a Gaussian. Due to the isotropic filter kernel, the second derivatives $\mathbf{G}_{uv}$ and $\mathbf{G}_{vu}$ are equal. When the image $\mathbf{I}(u,v)$ is convolved with the second order Gaussian derivative, for example in u-direction, we get $\mathbf{I}_{uu}(u,v)$ as

$$\mathbf{I}_{uu}(u,v) = \mathbf{I}(u,v) * \mathbf{G}_{uu}(u,v). \tag{1}$$

Similar definitions apply for $\mathbf{I}_{vv}(u,v)$ and $\mathbf{I}_{uv}(u,v)$. Next, the eigenvalues of the Hessian matrix $\mathbf{H}(u,v) \in \mathbb{R}^{2\times 2}$ are calculated by

$$\eta(u,v)_{1,2} = \frac{\mathbf{I}_{uu}+\mathbf{I}_{vv} \pm \sqrt{(\mathbf{I}_{uu}+\mathbf{I}_{vv})^2 - 4\left(\mathbf{I}_{uu}\cdot\mathbf{I}_{vv} - \mathbf{I}_{uv}^2\right)}}{2}, \tag{2}$$

where $\eta_1(u,v) \in \mathbb{R}$ and $\eta_2(u,v) \in \mathbb{R}$ denote the eigenvalues of the Hessian matrix $\mathbf{H}$. For the blob detection we look for the highest eigenvalues and define them as candidates for the cryo-balloon catheter marker. Currently, the 300 strongest eigenvalues, blobs $\mathbf{b}_i = (u_i, v_i)$ are considered as candidates for the X-ray marker of the cryo-balloon catheter. From this initial set, candidates that are close to the image boundaries are excluded as well as candidates that occur only sparsely in a region, or clustered blobs. Below, we explain how to identify the correct X-ray marker.

### B. Feature Computation

In the next step, the following features are computed for each X-ray marker candidate. The first feature $f_1$ is the eigenvalue of the blob $f_1 = \eta_1(\mathbf{b}_i) \in \mathbb{R}$. For the second feature $f_2$, the average image intensity in a small region $\delta_1$

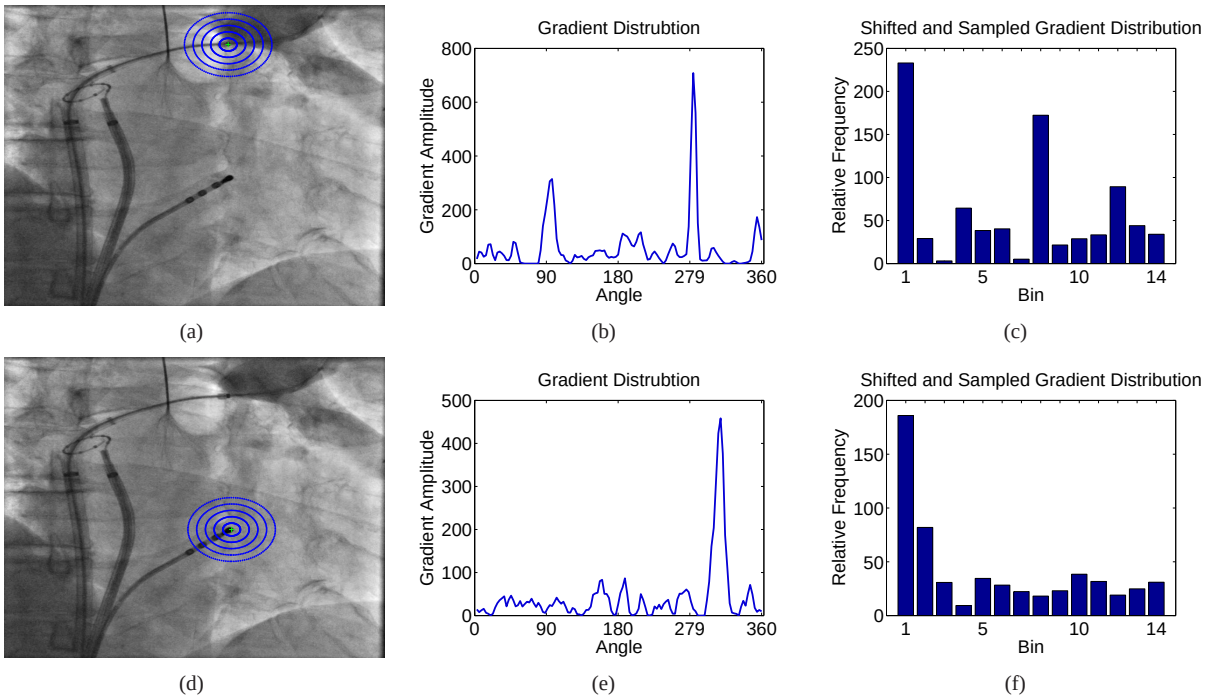


Fig. 2. Example images for the feature describing the circular gradient environment around a X-ray marker candidate. (a) Marker candidate set on the actual X-ray marker of the cryo-balloon catheter. (d) Marker candidate on a coronary sinus catheter. (a) and (d): Images with a set of gradient circles, where $r_k = r_5$. (b) and (e): Gradient distribution around each marker, displayed as the average of the function $\mathbf{I}(\mathbf{p}(\theta, r_k))$ for all radii $r_k$, where (b) corresponds to the cryo-balloon marker and (e) to the coronary sinus marker candidate. (c) and (f): Average sampled function $\mathbf{I}(\mathbf{p}(\theta, r_k))$ after shifting the function values to the most prominent gradient location to achieve invariance to rotation, with an interval size of $\iota = 14$, where (c) corresponds to the cryo-balloon marker and (f) to the coronary sinus marker candidate.

around the marker candidate is computed as follows,

$$f_2 = m_d(\mathbf{b}_i) = \sum_{u=b_u-\delta_1}^{b_u+\delta_1} \sum_{v=b_v-\delta_1}^{b_v+\delta_1} \mathbf{I}(u, v), \tag{3}$$

with $f_2 \in \mathbb{R}$. The area should contain only dark values, as the area's size is set to the size of the actual catheter marker. As a third feature $f_3$, we use a larger region $\delta_2$ to compute the average intensity,

$$f_3 = m_h(\mathbf{b}_i) = \sum_{u=b_u-\delta_2}^{b_u+\delta_2} \sum_{v=b_v-\delta_2}^{b_v+\delta_2} \mathbf{I}(u, v), \tag{4}$$

with $f_3 \in \mathbb{R}$. This region should contain more bright pixels as the inflated balloon catheter is less dense than the surrounding blood. The fourth feature $f_4$ is the difference of the bright area $m_h(\mathbf{b}_i)$ and the dark area $m_d(\mathbf{b}_i)$. This feature differentiates the radio-opaque marker of the cryo-balloon catheter from the other possible candidates. The inflated balloon appears brighter in the fluoroscopic image as it displaces the surrounding blood. As density of nitrogen is lower compared to blood, the X-ray attenuation is lower for the cryo-balloon. The X-ray marker, however, is made of very dense material to appear opaque in the image. Therefore the difference of these two areas is a unique feature regarding the cryothermal balloon catheter. The cryo-catheter marker is attached beyond the balloon's center, towards the distal third of the cryo-balloon. Also, there is a guide-wire or lasso-catheter which continues past the marker. This differentiates a cryo-balloon catheter from other catheters such as ablation or mapping catheters that can be present in the fluoroscopic images as well. For these catheters, the electrodes are placed at the end of the catheter or in a circular arrangement. Unfortunately, the electrodes of these catheters also have a prominent blob-like structure. These catheter properties lead us to design a feature that describes the presence and spatial arrangements of catheters in the area around each possible marker $\mathbf{b}_i$. See Fig. 2 (a) and (d) for an illustration. In particular, we evaluate the circular distribution of gradients around a potential cryo-balloon X-ray marker. Feature computation comprises the following steps. First, for each possible marker $\mathbf{b}_i$ five circles with different radii $r_k = r_5 \in \{20, 40, 60, 80, 100\}$ (in pixels) are defined. In the parametric form, these circles are expressed as a set of points $\mathbf{p}(\theta, r_k) = (u_c, v_c)$ such that $u_c = u_i + r_k \cos\theta$ and $v_c = v_i + r_k \sin\theta$ with $\theta \in [0, 2\pi]$. The circles $\mathbf{I}(\mathbf{p}(\theta, r_k))$ can be interpreted as a one-dimensional function of gray-scale intensities. Examples can be seen in Fig. 2 (b) and (e). The circle $\mathbf{I}(\mathbf{p}(t, r_k))$ is subsequently smoothed with a one-dimensional Gaussian kernel $G_{1-D}(\sigma_G, \mathbf{p}(t, r_k))$ with a $\sigma_G = 0.5$ to eliminate remaining image noise. Then, it is convolved with a one-dimensional Logarithm-of-Gaussian kernel $L_{1-D}(\sigma_L, \mathbf{p}(\theta, r_k))$ with $\sigma_L = 0.8$ to highlight areas of rapid intensity change, i. e. edges. The resulting function represents the circular distribution of edges around a possible marker $\mathbf{b}_i$. The resulting functions of each circle are averaged over all $r_k$ and the resulting averaged function is sub-sampled into $\iota = 14$ intervals. This decreases then number of features, lowers their sensitivity to noise, and facilitates a faster computation time.

As the catheters may occur in the image in arbitrary

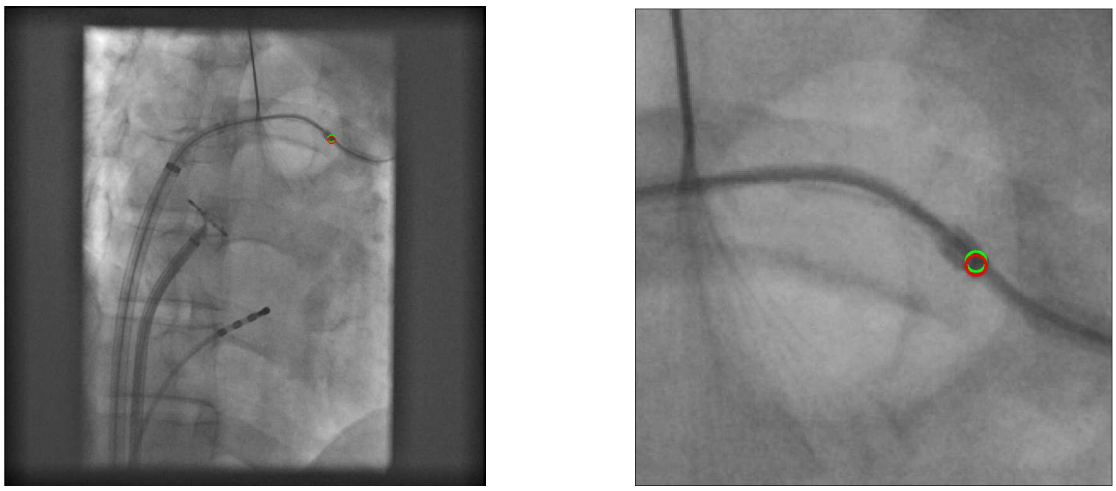

(a) (b)

Fig. 3. Example for cryo-balloon catheter detection. (a) Result of our cryo-balloon catheter detection for plane A. (b) Zoomed-in version of (a). Our detection result is shown in red and the gold-standard annotation in green.

orientation, the features need to be invariant to rotation [27]. To this end, the 14 intervals are shifted such that the interval associated with the highest filter response is always at the first position, which are declared as features $f_5$ to $f_{18}$. See Fig. 2 (c) and (f) for an illustration. The 14 intervals $f_5$ to $f_{18}$ along with the eigenvalue of the blob $f_1$, the average of the small region $f_2$, the average of the larger region $f_3$, the difference of the regions $f_4$ are all used as features for the SVM classification explained next.

### C. Feature Classification

For each of the $n$ potential markers $\mathbf{b}_i$, the 18 features previously described are computed. A kernel-SVM with a radial basis function kernel is used to classify the marker candidates [28]. The result of the classification for one test image is a ranking $\kappa(\mathbf{b}_i)$ and class-prediction $\omega(\mathbf{b}_i) \in \mathbb{R}$ for each candidate $\mathbf{b}_i$. As multiple $\mathbf{b}_i$ within one image might be classified as the cryo-marker, $\text{sign}(\omega(\mathbf{b}_i)) = +1$, an additional step needs to be performed to make a final decision on the predicted cryo-marker position in the image. To this end, a binary map, based on $\text{sign}(\omega(\mathbf{b}_i)) = +1$, of the same size as the original image is computed. On this binary map a 4-connectivity search is performed for all marker candidates resulting in connected groups $\mathcal{A}_k$ with $k = 1, \ldots, n_g$ where $n_g$ is the number of groups, which varies from image to image. Each group is assigned a score that is based on the classification ranks $\kappa(\mathbf{b}_i)$ of all $\mathbf{b}_i$ geometrically related to a group $\mathcal{A}_k$ by

$$s_k = \frac{1}{n_g} \sum_{\mathbf{b}_i \in \mathcal{A}_k} \kappa(\mathbf{b}_i) \tag{5}$$

The group $\mathcal{A}_k$ with the highest score $s_k$ is considered to be the actual cryo-balloon X-ray marker, where the geometric center of $\mathcal{A}_k$ is the position of the cryo-marker in the image, referred to as $\mathbf{b}$. An example of our catheter detection for plane A RAO view is displayed in Fig. 3.

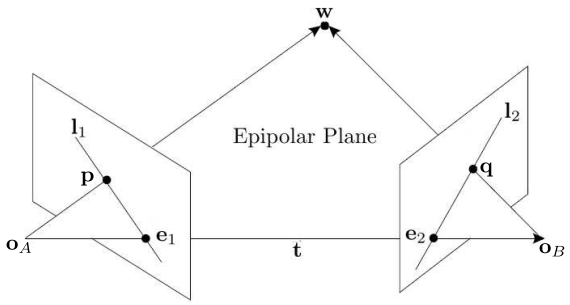


Fig. 4. The epipolar geometry with the two optical centers (X-ray sources) $\mathbf{o}_A$ and $\mathbf{o}_B$ for each image plane. The translation vector $\mathbf{t}$ from image plane A to image plane B. Point $\mathbf{p}$ is the 2-D image point in image A and $\mathbf{q}$ is the 2-D image point in image B and the associated 3-D point is $\mathbf{w}$. $\mathbf{l}_1$ is the epipolarline in image A and the corresponding epipole is $\mathbf{e}_1$, $\mathbf{l}_2$ is the epipolarline in image B with the corresponding epipole $\mathbf{e}_2$.

### D. Catheter Localization in 3-D

The detected cryo-balloon catheter marker is denoted as $\mathbf{b}$. As the cryo-balloon catheter localization is performed using biplane images as input, the blob has to be detected in plane A (RAO view) and plane B (LAO view). There are two possible ways to find the corresponding X-ray marker of the cryo-balloon catheter in plane B. Either the whole cryo-balloon catheter detection is performed for both planes resulting in $\mathbf{b}_A$ and $\mathbf{b}_B$. Or the X-ray marker in plane B can be found by looking for the closest corresponding point to $\mathbf{b}_A$ in the set of possible X-ray marker candidates $\mathbf{b}_{B,i}$ using the epipolar constraints [29]. The set $\mathbf{b}_{B,i}$ contains all possible X-ray marker candidates after the exclusion of blobs with a certain margin to the image boundary in plane B.

In general, the epipolar constraint exists between any two camera systems. Consider the case of two cameras depicted in Fig. 4. Let $\mathbf{o}_A \in \mathbb{R}^3$ be the optical center of camera A and $\mathbf{o}_B \in \mathbb{R}^3$ the optical center of camera B. Given a 3-D point $\mathbf{w} \in \mathbb{R}^3$ and its 2-D projections $\mathbf{p}$ and $\mathbf{q} \in \mathbb{R}^2$ both points are

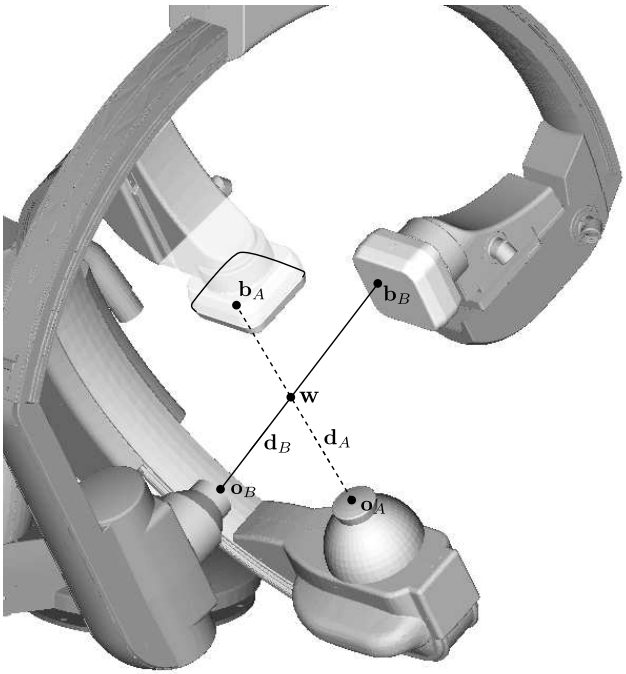


Fig. 5. The projection geometry of a biplane C-arm system. With the two optical centers $\mathbf{o}_A$ and $\mathbf{o}_B$ for each image plane and the corresponding direction vector $\mathbf{d}_A$ and $\mathbf{d}_B$. Knowing the projection matrix $\mathbf{P}$ and the two 2-D cryo-balloon X-ray marker $\mathbf{b}_A$ and $\mathbf{b}_B$, the 3-D point $\mathbf{w}$ can be computed. The optical centers do not represent their true locations but have been put on the outside of the tube collimator covers for purpose of illustration.

related to a projective transform given as

$$s\mathbf{p} = \mathbf{P}\mathbf{w} \tag{6}$$

where $s$ is a scale factor and $\mathbf{P} \in \mathbb{R}^{3\times4}$ is the projection matrix [30].

The epipolar geometry defines the geometry between the two cameras (in our case X-ray sources) creating a stereoscopic system. Given a point $\mathbf{w} \in \mathbb{R}^3$ and its 2-D projections $\mathbf{p}$ and $\mathbf{q}$ $\in \mathbb{R}^2$ on both image planes, the three points define the epipolar plane, which intersects both images at the epipolar lines $\mathbf{l}_1$ and $\mathbf{l}_2 \in \mathbb{R}^3$, as shown in Fig. 4. Moreover, the intersections of all epipolar lines define an epipole on both image planes, denoted by $\mathbf{e}_1$ and $\mathbf{e}_2 \in \mathbb{R}^2$. For a more detailed description of the epipolar geometry please see Armangué et al. [31].

The epipolar geometry is required to find the corresponding blob $\mathbf{b}_B$ to $\mathbf{b}_A$ from the set $\mathbf{b}_{B,i}$. To do so, the epipolarline $\mathbf{l}_2$ is computed for the tip estimate $\mathbf{b}_A$. Given the set $\mathbf{b}_{B,i}$ and the epipolarline $\mathbf{l}_2$, the tip estimate $\mathbf{b}_B$ is determined by

$$\mathbf{b}_B = \arg\min_{\mathbf{b}_j \in \mathbf{b}_{B,i}} \left|\mathbf{l}_2^T \cdot \mathbf{b}_j\right|. \tag{7}$$

However, if the first localization in plane A is wrong, the detection of the radio-opaque marker in plane B using epipolar constraints will be also wrong. This is why it is a good idea to start with the image which has the better image quality. In many cases, this is the image obtained with a view angle closer to the posterior-anterior view direction, e.g., 30° RAO.

After the position of the X-ray marker is known in plane A and B, the 3-D position can be calculated. For this, the projection geometry of the C-arm system has to be known. The projection matrices can be obtained analytically, assuming an ideal geometric model of the C-arm, or by calibration, taking into account the non-ideal behavior of the C-arm system's projection geometry [29], [32]. Modern C-arm systems are calibrated, such their matrices are known [33].

The projection geometry of a C-arm system is similar to the geometry of a pinhole camera, thus a perspective projection is considered. For a more detailed description of the projection geometry of a C-arm system, see Brost et al. [34].

This means a 3-D point $\mathbf{w} \in \mathbb{R}^3$ can be projected onto the image plane, resulting in $\mathbf{p} \in \mathbb{R}^2$ knowing the projection matrix $\mathbf{P} \in \mathbb{R}^{3\times4}$, by

$$\tilde{\mathbf{p}} = \mathbf{P}\tilde{\mathbf{w}} = \mathbf{K}[\mathbf{R}|\mathbf{t}]\tilde{\mathbf{w}}, \tag{8}$$

where the $\tilde{}$ denotes the homogeneous coordinates of the points, $\mathbf{K} \in \mathbb{R}^{3\times3}$ is the intrinsic camera matrix, $\mathbf{R} \in \mathbb{R}^{3\times3}$ the rotation matrix of the camera and $\mathbf{t} \in \mathbb{R}^3$ the translation vector of the camera. As a biplane system is considered, the projection matrices are denoted as $\mathbf{P}_A$ for plane A and $\mathbf{P}_B$ for plane B, respectively.

Having the 2-D cryo-balloon X-ray marker in plane A, denoted as $\mathbf{b}_A$ and the projection matrix $\mathbf{P}_A$ for plane A the equation can be rewritten as

$$\widetilde{\mathbf{b}}_A = \mathbf{K}_A(\mathbf{R}_A \cdot \widetilde{\mathbf{w}} + \mathbf{t}_A). \tag{9}$$

As the image point $\mathbf{b}_A$ is given in homogeneous coordinates, the exact coordinates of the points are known up to a scaling factor $\lambda \in \mathbf{R}$. This fact can be used to construct a line through the 2-D image point and the point in 3-D. A point along this line is described by

$$\mathbf{r}_A(\lambda) = \lambda \cdot \mathbf{R}_A^{-1}\mathbf{K}_A^{-1}\widetilde{\mathbf{b}}_A - \mathbf{R}_A^{-1} \cdot \mathbf{t}_A. \tag{10}$$

Substituting the point of the origin $\mathbf{o}_A = -\mathbf{R}_A{}^{-1} \cdot \mathbf{t}_A$ and the direction $\mathbf{d}_A = \mathbf{R}_A{}^{-1}\ \mathbf{K}_A{}^{-1}\ \widetilde{\mathbf{b}}_A$, Eq. (10) can be rewritten as

$$\mathbf{r}_A(\lambda) = \mathbf{o}_A + \lambda \cdot \mathbf{d}_A. \tag{11}$$

Given the two 2-D cryo-balloon marker in plane A, $\mathbf{b}_A$, and plane B, $\mathbf{b}_B$, two ray equations can be computed. Due to errors during the localization of the cryo-balloon tip in 2-D projections associated with the same 3-D object, the lines do not necessarily intersect. As both rays, $\mathbf{r}_A$ and $\mathbf{r}_B$, represent the same point in 3-D. The final point in 3-D is computed by

$$\mathbf{w}^\star = \frac{1}{2} \cdot (\mathbf{o}_A + \hat{\lambda}\mathbf{d}_A + \mathbf{o}_B + \hat{\mu}\mathbf{d}_B), \tag{12}$$

where $\hat{\mu}$ is the scaling parameter for $\mathbf{r}_B$, equivalent to $\hat{\lambda}$ for $\mathbf{r}_A$. The scaling parameters were estimated from the intersection of the two rays using singular value decomposition. See Fig. 5 for an illustration of the 3-D projection geometry of a biplane C-arm system. For details of the point localization see Brost et al. [32].

## IV. Evaluation and Results

In this section we evaluate our proposed method. The goal of the evaluation is to show that the detection in 2-D and the reconstruction in 3-D are satisfactory for clinical use. Our data comprised 150 monoplane images from 75

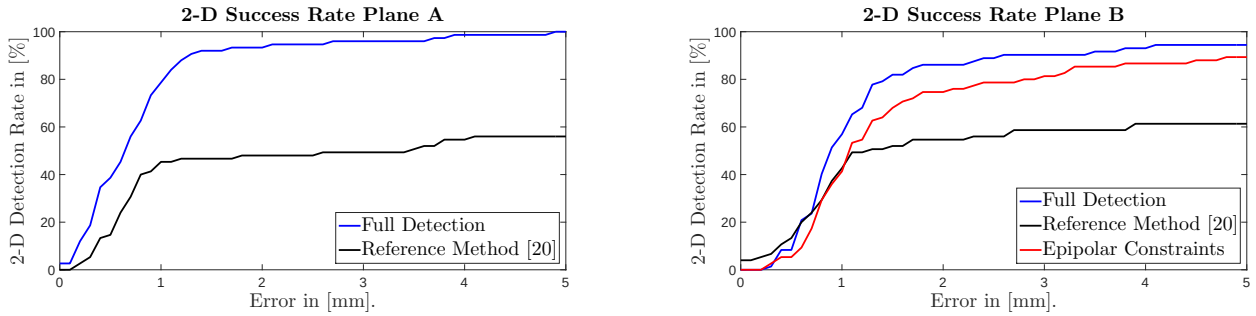


(a) (b)

Fig. 6. (a) The cryo-balloon catheter detection in 2-D yielded an average error of 1.00 mm ± 0.82 mm with a total minimum of 0.00 mm and a total maximum of 4.88 mm in plane A (RAO view). The previous method yielded an average error of 1.03 mm ± 1.08 mm with a total minimum of 0.17 mm and a total maximum of 4.04 mm in plane A. (b) The cryo-balloon catheter detection in 2-D yielded an average error of 1.13 mm ± 0.24 mm with a total minimum of 0.24 mm and a total maximum of 4.10 mm in plane B (LAO view) with the full detection algorithm. Applying epipolar constraints for marker detection in plane B, we obtained an average error of 1.18 mm ± 0.99 mm and an overall maximum error of 4.75 mm and an overall minimum error of 0.00 mm. The previous method yielded an average error of 0.98 mm ± 0.84 mm with a total minimum of 0.17 mm and a total maximum of 3.83 mm in plane B. Plane A was at an angle of 30° RAO, plane B had an angle of 60° LAO.

| **Detection Error in 2-D** | | | | | |
|---|---|---|---|---|---|
| | **Plane A** | | **Plane B** | | |
| | Our Approach | [20] | Our Approach | Epipolar Approach | [20] |
| Mean | 1.00 mm | 1.03 mm | 1.13 mm | 1.18 mm | 0.98 mm |
| Max | 4.88 mm | 4.04 mm | 4.10 mm | 4.75 mm | 3.83 mm |
| Success | 99.0 % | 56.0 % | 90.6 % | 89.3 % | 61.3 % |

TABLE I
COMPARISON OF THE DETECTION RATE AND ERROR OF OUR APPROACH TO THE PREVIOUS METHOD [20].

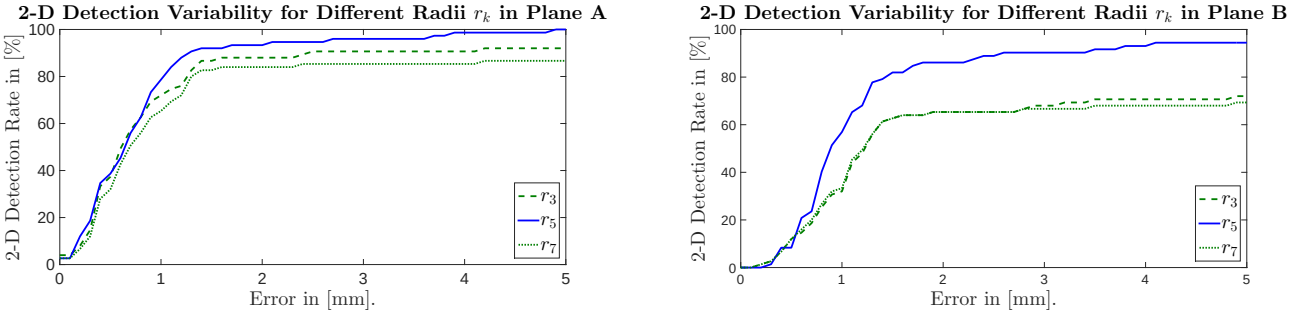


(a) (b)

Fig. 7. Variability evaluation of different radii, where $r_3 \in \{20, 40, 60\}$, $r_5 \in \{20, 40, 60, 80, 100\}$ and $r_7 \in \{20, 40, 60, 80, 100, 120, 140\}$. (a) The cryo-balloon detection for plane A achieved a detection rate of 99.0 % using $r_5$. For $r_3$ we achieved a detection rate of 92.0 % and for $r_7$ 86.7 %. The best result was achieved using $r_5$. (b) The cryo-balloon detection for plane B achieved a detection rate of 90.6 % using $r_5$. For $r_3$ we achieved a detection rate of 72.0 % and for $r_7$ 69.3 %. The evaluation shows, that adding or removing radii deteriorates the accuracy of our proposed method. The best result was achieved using $r_5$.

biplane sequences acquired over 40 different patients from two clinical sites. The catheter setup for cryo-balloon procedures involved one circumferential mapping catheter, one catheter in the coronary sinus and one cryo-balloon catheter. For the evaluation, only data of procedures involving the first and second generation cryo-balloon catheters were available to us. The cryothermal balloon catheter was placed at the ostium of the pulmonary vein during image acquisition. The catheter is usually firmly placed to ensure a good wall contact. A suboptimal wall contact may lead to incomplete pulmonary vein isolation. Some images also show ECG leads that were attached to the skin of the patient or temperature probes inside the esophagus. All images were acquired on a Siemens Artis zee biplane system (Siemens Healthcare GmbH, Forchheim, Germany). For evaluation of our method, a gold-standard annotation of the radio-opaque marker was available, provided by an electrophysiologist. The evaluation itself was performed by a leave-one-out cross validation, i. e. one sequence was excluded from training of the classifier and used for testing. Given the gold-standard annotation, the Euclidean distance between our detection result and the gold-standard annotation was computed as 2-D detection error. As 5 mm is mostly used as a clinically acceptable threshold, our method has a detection success rate of 99.0 % in plane A (RAO). For

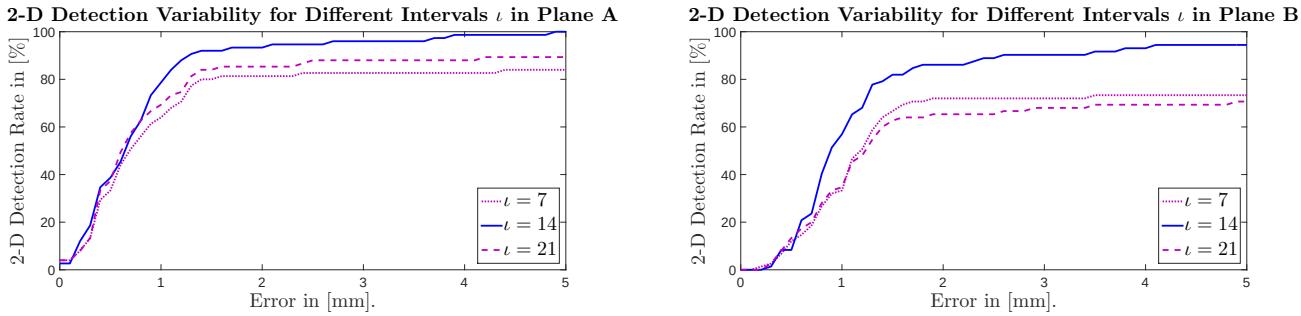


Fig. 8. Variability evaluation for different interval sizes $\iota$ of the gradient distribution around each possible marker. Changing the number of intervals, automatically changes the number of features used for the SVM. (a) The cryo-balloon detection for plane A achieved a detection rate of 99.0 % using an interval size of $\iota = 14$. For $\iota = 7$ we achieved a detection rate of 84.0 % and for $\iota = 21$ 89.3 %. Changing $\iota = 7$ smooths the gardient distribution too much, therefore the classification result is reduced. Increasing $\iota = 21$ leads to an overestimate of the gradient distribution and also decreases the classification result. The optimal result was achieved with an interval size of $\iota = 14$. (b) The cryo-balloon detection for plane B achieved a detection rate of 90.6 % using an interval size of $\iota = 14$. For $\iota = 7$ we achieved a detection rate of 73.3 % and for $\iota = 21$ 70.3 %, respectively.

plane B (LAO), we have a success rate of 90.6 % when applying the multi-step blob detection algorithm and a success rate of 89.3 % when applying epipolar constraints for the detection. Excluding detection failures, our method yielded a detection error of 1.00 mm $\pm$ 0.82 mm in plane A. The results for plane A are shown in Fig. 6 (a). In plane B we achieved a detection accuracy of 1.13 mm $\pm$ 0.24 mm using the whole detection algorithm and 1.18 mm $\pm$ 0.99 mm using the epipolar constraints. Fig. 6 (b) states the results of the two detection methods for plane B. On the same data set, our previous method [20] yielded a success rate of 56.0 % in plane A and of 61.3 % in plane B. For plane A, it achieved an average error of 1.03 mm $\pm$ 1.08 mm with an overall maximum error of 4.04 mm and an overall minimum error of 0.17 mm. For plane B, an average error of 0.98 mm $\pm$ 0.84 mm with an overall maximum error of 3.83 mm and an overall minimum error of 0.17 mm were achieved. Note that only correctly detected radio-opaque markers were used for the error computation. This is the reason why the errors of the two methods are similar, but the detection rates are different. A direct comparison between the previous method and our novel approach is given in Table I. The main technical difference between the proposed method and the previous method [20] is, that only a cost-function was used in the earlier method to identify the cryo-balloon marker. Furthermore, the marker was only detected in a single plane, so no 3-D localization was possible. In this work, on the other hand, a machine learning approach was used to find the X-ray marker of the cryo-balloon catheter

For the feature computation, several parameters were set. First, for each possible marker $\mathbf{b}_i$ different sets of radii $r_k$ were defined. A comparison of different number of radii $r_k$ and their impact on the results is given in Fig. 7, were $r_3 \in \{20, 40, 60\}$, $r_5 \in \{20, 40, 60, 80, 100\}$ and $r_7 \in \{20, 40, 60, 80, 100, 120, 140\}$. The cryo-balloon detection for plane A achieved a detection rate of 99.0 % using $r_5$. For $r_3$ we achieved a detection rate of 92.0 % and for $r_7$ 86.7 %. For plane B we achieved a detection rate of 90.6 % using $r_5$. For $r_3$ we achieved a detection rate of 72.0 % and for $r_7$ 69.3 %. The best results were achieved using $r_5$. This can be explained mathematically. The most often used cryo-balloon had a diameter of 28 mm. Knowing the pixel spacing $\delta_p = 0.1725$ of the fluoroscopic images and the diameter of the cryo-balloon, it results in a length of 162 pixels. As the radio-opaque marker of the cryo-balloon catheter is positioned in the first third of the balloon, we can make sure that we cover a lot of the balloon, especially regarding the distal end. Another parameter was the number of intervals $\iota$ for the gradient distribution around each possible marker. An evaluation of the impact for different interval sizes $\iota$ is given in Fig. 8. Changing the number of intervals automatically changes the number of features used for the SVM. The cryo-balloon detection for plane A achieved a detection rate of 99.0 % using an interval size of $\iota = 14$. For $\iota = 7$ we achieved a detection rate of 84.0 % and for $\iota = 21$ 89.3 %. For plane B we achieved a detection rate of 90.6 % using $\iota = 14$. For $\iota = 7$ we achieved a detection rate of 73.3 % and for $\iota = 21$ 70.7 %. Changing $\iota = 7$ smooths the gradient distribution too much, therefore the classification result is reduced. Increasing $\iota = 21$ leads to an overestimate of the gradient distribution and also decreases the classification result. The optimal result was achieved with an interval size of $\iota = 14$.

As biplane sequences were available, localization in 3-D could be performed by triangulation. Unfortunately, an evaluation in 3-D would require additional 3-D ground truth. As neither a 3-D data set nor 3-D information from an electromagnetic navigation system was available, only an estimate of the 3-D error could be calculated. To do so, we used the gold-standard annotation provided by an electrophysiologist to perform a 3-D point localization based on the two 2-D ground truth annotations. To estimate the 3-D error of our localization method, we computed the Euclidean distance between the gold-standard triangulation result and the localized cryo-balloon marker in 3-D. On average, our method yielded a 3-D localization error of 0.36 mm $\pm$ 0.86 mm, with an overall maximum error of 4.97 mm and an overall minimum error of 0.03 mm. Using the same 5 mm threshold as for the detection of the marker on a single plane image, the localization success rate was found to be 97.3 %. As the previous method achieved only a 3-D success rate of 56.0 % and 61.3 % a comparison

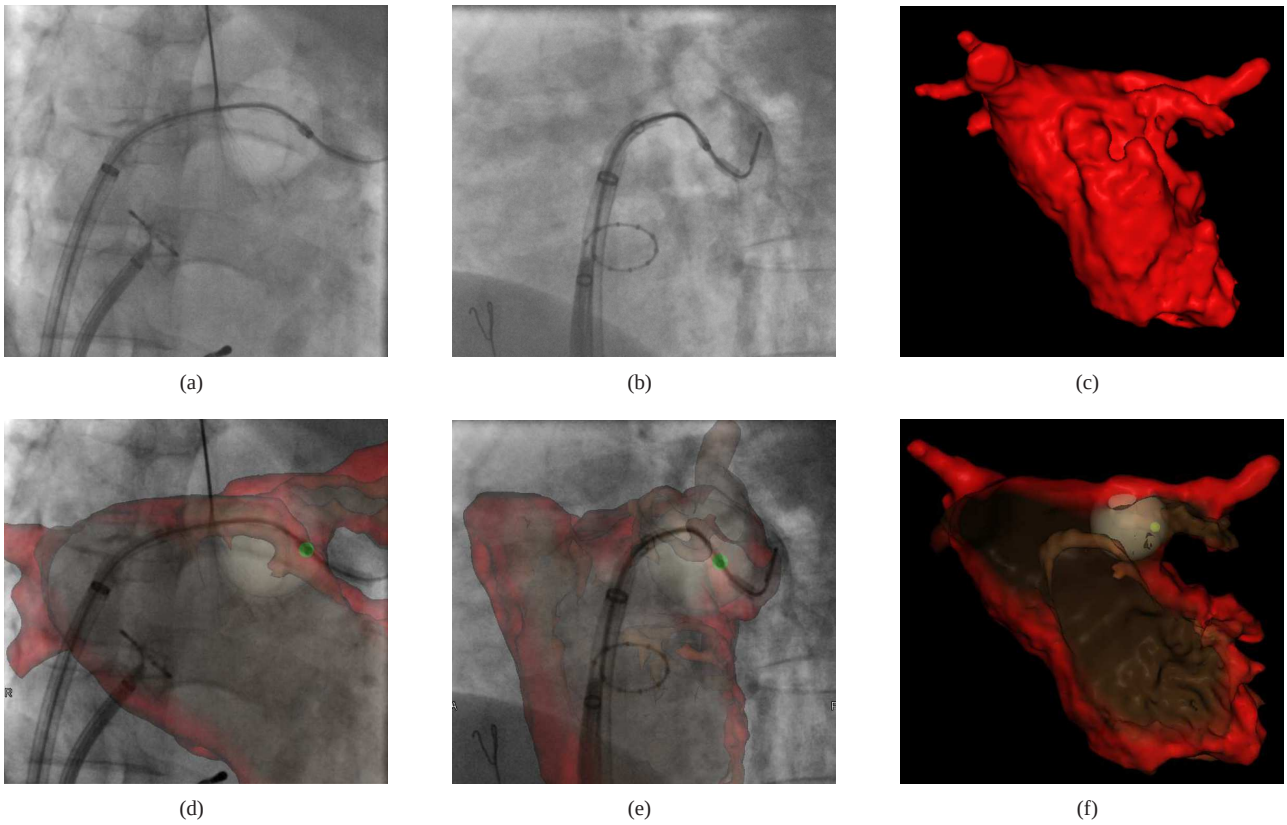

Fig. 9. Example of the cryo-balloon localization in 3-D. (a) Input image of plane A. (b) Input image of plane B. (c) 3-D surface mesh of the left atrium. (d) Result of our cryo-balloon catheter detection in image plane A, overlayed with the 3-D surface mesh from (c). (e) Result of the detection in image plane B, overlayed with the 3-D surface from (c). (f) Example for cryo-balloon localization in 3-D. Position of the automatically localized cryo-balloon catheter in 3-D with respect to a pre-planned position of the cryo-balloon catheter using AFiT [35].

in 3-D was omitted.

## V. Discussion and Conclusions

Our new method clearly outperforms the previous method [20] with 2-D success rates of 99.0 % vs. 56.0 % and 90.6 % vs. 61.3 %, respectively. The results for image plane B (LAO) are in general worse than for plane A (RAO). This can be attributed to the fact that plane B is positioned in a more lateral orientation, while plane A is positioned closer to an anterior-posterior view direction. In our clinical set-up, plane A was at an angle of $30°$ RAO and plane B had an angle of $60°$ LAO. As a consequence, both effective patient thickness and the scatter for image plane B are higher, resulting in a lower image quality. See Fig. 10 for an illustration of the clinical setup of the C-arm system. Our approach failed in 1.0 % out of the 75 sequences for image plane A and in 9.4 % for image plane B. We considered a detection result a failure if the Euclidean distance between the detected marker and the gold-standard annotation was larger than 5.0 mm. In the remaining frames, our method achieved a 2-D detection error of 1.00 mm $\pm$ 0.82 mm for plane A and 1.13 mm $\pm$ 0.24 mm for plane B. An example of our catheter detection for plane A is displayed in Fig. 3.

The higher number of failures in image plane B using the epipolar-constraint to find the correct marker position in image plane B can be explained as follows. Given a wrong marker position in plane A, the correct marker position in image plane B cannot be found. This is a main drawback of the epipolar method. One could, however, consider changing the C-arm view angles to $45°$ and $45°$ in both RAO and LAO. Then one could apply the multi-step blob detection in both views and pick the better result. Our method was evaluated using the first and second generation of cryo-balloon catheters. Recently, a third generation of cryo-balloon catheters was introduced with a shorter tip. Since there is still a radio-opaque marker inside the cryo-balloon catheter, the catheter specific features can again be calculated and our algorithm be applied. Some parameter changes may, however, be necessary.

As biplane images were available, an estimate of the 3-D position of the cryo-balloon catheter marker could be computed. The 3-D position could then be visualized with respect to a pre-operative data set of the left atrium as, e.g., used for planning purposes [36], [35]. The localized marker of the cryo-balloon then facilitates the verification of the balloon catheter position as illustrated in Fig. 9 (f). Furthermore, our method can be used to either initialize localization methods or as a tracking method on its own [37] - either in 2-D or even in 3-D, if the X-ray markers are detected in the images simultaneously acquired on a biplane X-ray system.

The automatic detection of the radio-opaque marker of the cryo-balloon catheter can also be used as the initialization point for the method presented by Hoffmann et al. [26]. From

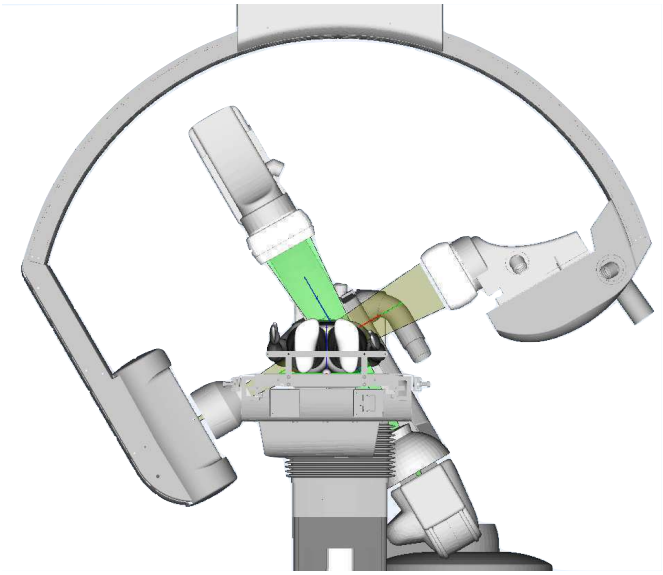

Fig. 10. Projection angles of the C-arm system. In our clinical set-up, plane A was at an angle of 30° RAO, depicted as the green ray and plane B had an angle of 60° LAO, represented by the yellow ray. As the amount of scatter is related to the patient width in X-ray view direction, its impact in the 30° RAO view direction is less than in 60° LAO view direction. This is one important reason why the A-plane image quality is better then its B-plane counterpart.

there we would get a 3-D model of the catheter shaft. Knowing the vector of the shaft, the 3-D position of the X-ray marker and the diameter of the cryo-balloon, a 3-D model of the cryo-balloon can be reconstructed and overlaid on the fluoroscopic images, see Fig. 9 (d) and (e) for an example. Several studies have already been published explaining how cryo-balloon ablation procedures can benefit from the visualization of the balloon catheter [38], [39]. However, all the workflows presented so far all require manual user interaction.

In the course of this work it has been shown that the cryo-balloon catheter detection in 2-D and the localization in 3-D using a blob-based support-vector-machine is possible.

## Research Disclaimer

The methods and information presented in this paper are based on research and are not commercially available.

## References


[1] A. Camm, P. Kirchhof, G. Lip, U. Schotten, I. Savelieva, S. Ernst, I. van Gelder, N. Al-Attar, G. Hindricks, B. Prendergast, H. Heidbüchel, O. Alfieri, A. Angelini, D. Atar, P. Colonna, R. de Caterina, J. de Sutter, A. Goette, B. Gorenek, M. Heldal, S. Hohloser, P. Kolh, J.-Y. L. Heuzey, P. Ponikowski, and F. Rutten, "Guidelines for the management of atrial fibrillation: The Task Force for the Management of Atrial Fibrillation of the European Society of Cardiology (ESC)," *European Heart Journal*, vol. 31, no. 19, pp. 2369–2429, October 2010.

[2] O. M. Wazni, N. F. Marrouche, D. O. Martin, A. Verma, M. Bhargava, W. Saliba, D. Bash, R. Schweikert, J. Brachmann, J. Gunther *et al.*, "Radiofrequency Ablation vs Antiarrhythmic Drugs as First-line Treatment of Symptomatic Atrial Fibrillation: A Randomized Trial," *The Journal of the American Medical Association*, vol. 293, no. 21, pp. 2634–2640, June 2005.

[3] G. Mugnai, G.-B. Chierchia, C. de Asmundis, J. Sieira-Moret, G. Conte, L. Capulzini, K. Wauters, M. Rodriguez-Mañero, G. Di Giovanni, G. Baltogiannis *et al.*, "Comparison of Pulmonary Vein Isolation Using Cryoballoon Versus Conventional Radiofrequency for Paroxysmal Atrial Fibrillation," *The American Journal of Cardiology*, vol. 113, no. 9, pp. 1509–1513, May 2014.

[4] A. J. Camm, G. Y. Lip, R. De Caterina, I. Savelieva, D. Atar, S. H. Hohnloser, G. Hindricks, P. Kirchhof, J. J. Bax, H. Baumgartner *et al.*, "2012 focused update of the ESC Guidelines for the management of atrial fibrillation," *European Heart Journal*, vol. 33, no. 21, pp. 2719–2747, August 2012.

[5] C. T. January, L. S. Wann, J. S. Alpert, H. Calkins, J. E. Cigarroa, and J. C. Cleveland, "2014 AHA/ACC/HRS Guideline for the Management of Patients With Atrial Fibrillation," *Journal of the American College of Cardiology*, vol. 64, no. 21, pp. e1–e76, December 2014.

[6] H. Calkins, K. H. Kuck, R. Cappato, J. Brugada, A. J. Camm, S.-A. Chen, H. J. Crijns, R. J. Damiano, D. W. Davies, J. DiMarco *et al.*, "2012 HRS/EHRA/ECAS Expert Consensus Statement on Catheter and Surgical Ablation of Atrial Fibrillation: Recommendations for Patient Selection, Procedural Techniques, Patient Management and Follow-up, Definitions, Endpoints, and Research Trial Design," *Europace*, vol. 14, no. 4, pp. 528–606, March 2012.

[7] A. Natale, A. Raviele, A. AL-AHMAD, O. Alfieri, E. Aliot, J. Almendral, G. Breithardt, J. Brugada, H. Calkins, D. Callans *et al.*, "Venice Chart International Consensus Document on Ventricular Tachycardia/Ventricular Fibrillation Ablation," *Journal of Cardiovascular Electrophysiology*, vol. 21, no. 3, pp. 339–379, March 2010.

[8] V. Fuster, L. E. Rydén, D. S. Cannom, H. J. Crijns, A. B. Curtis, K. A. Ellenbogen, J. L. Halperin, J.-Y. Le Heuzey, G. N. Kay, J. E. Lowe *et al.*, "ACC/AHA/ESC 2006 Guidelines for the Management of Patients With Atrial Fibrillation," *Europace*, vol. 8, no. 9, pp. 651–745, June 2006.

[9] F. Gaita, J. F. Leclercq, B. Schumacher, M. Scaglione, E. Toso, F. Halimi, A. Schade, S. Froehner, V. Ziegler, D. Sergi *et al.*, "Incidence of Silent Cerebral Thromboembolic Lesions After Atrial Fibrillation Ablation May Change According to Technology Used: Comparison of Irrigated Radiofrequency, Multipolar Nonirrigated Catheter and Cryoballoon," *Journal of Cardiovascular Electrophysiology*, vol. 22, no. 9, pp. 961–968, September 2011.

[10] J. G. Andrade, P. Khairy, P. G. Guerra, M. W. Deyell, L. Rivard, L. Macle, B. Thibault, M. Talajic, D. Roy, and M. Dubuc, "Efficacy and safety of cryoballoon ablation for atrial fibrillation: A systematic review of published studies," *Heart Rhythm*, vol. 8, no. 9, pp. 1444–1451, November 2011.

[11] Y. van Belle, P. Janse, M. Rivero-Ayerza, A. Thornton, E. Jessurun, D. Theuns, and L. Jordaens, "Pulmonary vein isolation using an occluding cryoballoon for circumferential ablation: feasibility, complications, and short-term outcome," *European Heart Journal*, vol. 28, no. 18, pp. 2231–2237, September 2007.

[12] T. Neumann, J. Vogt, B. Schumacher, A. Dorszewski, M. Kuniss, H. Neuser, K. Kurzidim, A. Berkowitsch, M. Koller, J. Heintze *et al.*, "Circumferential Pulmonary Vein Isolation With the Cryoballoon Technique: Results From a Prospective 3-Center Study," *Journal of the American College of Cardiology*, vol. 52, no. 4, pp. 273–278, July 2008.

[13] S. Knecht, M. Khne, D. Altmann, P. Ammann, B. Schaer, S. Osswald, and C. Sticherling, "Anatomical Predictors for Acute and Mid-Term Success of Cryoballoon Ablation of Atrial Fibrillation Using the 28 mm Balloon," *Journal of Cardiovascular Electrophysiology*, vol. 24, no. 2, pp. 132–138, February 2013.

[14] M. L. Koller and B. Schumacher, "Cryoballoon ablation of paroxysmal atrial fibrillation: bigger is better and simpler is better," *European Heart Journal*, vol. 30, no. 6, pp. 636–637, February 2009.

[15] P. Defaye, A. Kane, A. Chaib, and P. Jacon, "Efficacy and safety of pulmonary veins isolation by cryoablation for the treatment of paroxysmal and persistent atrial fibrillation," *Europace*, vol. 13, no. 6, pp. 789–795, March 2011.

[16] B. Avitall, D. Urboniene, G. Rozmus, D. Lafontaine, R. Helms, and A. Urbonas, "New Cryotechnology for Electrical Isolation of the Pulmonary Veins," *Journal of Cardiovascular Electrophysiology*, vol. 14, no. 3, pp. 281–286, March 2003.

[17] S. Kumar, G. Brown, F. Sutherland, J. Morgan, D. Andrews, L.-H. Ling, A. McLellan, G. Lee, T. Robinson, P. Heck *et al.*, "The Transesophageal Echo Probe May Contribute to Esophageal Injury After Catheter Ablation for Paroxysmal Atrial Fibrillation Under General Anesthesia: A Preliminary Observation," *Journal of Cardiovascular Electrophysiology*, vol. 26, no. 2, pp. 119–126, February 2015.

[18] W. Su, R. Kowal, M. Kowalski, A. Metzner, J. T. Svinarich, K. Wheelan, and P. Wang, "Best practice guide for cryoballoon ablation in atrial fibrillation: The compilation experience of more than 3000 procedures," *Heart Rhythm*, July 2015.

[19] F. Bourier, D. Vukajlovic, A. Brost, J. Hornegger, N. Strobel, and K. Kurzidim, "Pulmonary Vein Isolation Supported by MRI-Derived 3D-Augmented Biplane Fluoroscopy: A Feasibility Study and a Quantitative Analysis of the Accuracy of the Technique," *Journal of Car-*

*diovascular Electrophysiology*, vol. 24, no. 2, pp. 113–120, February 2013.

[20] T. Kurzendorfer, A. Brost, C. Jakob, P. Mewes, F. Bourier, M. Koch, K. Kurzidim, J. Hornegger, and N. Strobel, "Cryo-Balloon Catheter Localization in Fluoroscopic Images," in *Proceedings of SPIE Medical Imaging 2013: Visualization, Image-Guided Procedures, and Modeling, Orlando, FL, USA, February 09–14*, February 2013.

[21] A. Brost, R. Liao, J. Hornegger, and N. Strobel, "3-D Respiratory Motion Compensation during EP Procedures by Image-Based 3-D Lasso Catheter Model Generation and Tracking," in *MICCAI 2009*, ser. LNCS, G. Yang, D. Hawkes, D. Rueckert, J. Noble, and C. Taylor, Eds. Springer Berlin / Heidelberg, September 2009, vol. 5761, pp. 394–401.

[22] A. Brost, R. Liao, N. Strobel, and J. Hornegger, "Respiratory motion compensation by model-based catheter tracking during EP procedures," *Medical Image Analysis*, vol. 14, no. 5, pp. 695–706, May 2010.

[23] A. Brost, A. Wimmer, R. Liao, F. Bourier, M. Koch, N. Strobel, K. Kurzidim, and J. Hornegger, "Constrained Registration for Motion Compensation in Atrial Fibrillation Ablation Procedures," *IEEE Transactions on Medical Imaging*, vol. 31, no. 4, pp. 870–881, April 2012.

[24] Y. Ma, A. King, N. Gogin, C. Rinaldi, J. Gill, R. Razavi, and K. Rhode, "Real-Time Respiratory Motion Correction for Cardiac Electrophysiology Procedures Using Image-Based Coronary Sinus Catheter Tracking," in *MICCAI 2010*, ser. LNCS, T. Jiang, N. Navab, J. Pluim, and M. Viergever, Eds., September 2010, vol. 6361, pp. 391–399.

[25] A. Brost, W. Wu, M. Koch, A. Wimmer, T. Chen, R. Liao, J. Hornegger, and N. Strobel, "Combined Cardiac and Respiratory Motion Compensation for Atrial Fibrillation Ablation Procedures," in *LNCS*, G. Fichtinger, A. Martel, and T. Peters, Eds., vol. 6891, Berlin/Heidelberg, September 2011.

[26] M. Hoffmann, A. Brost, C. Jakob, F. Bourier, M. Koch, K. Kurzidim, J. Hornegger, and N. Strobel, "Semi-Automatic Catheter Reconstruction from Two Views," in *MICCAI 2012, Part I*, ser. Lecture Notes in Computer Science, N. Ayache, H. Delingette, P. Golland, and K. Mori, Eds., Berlin, Heidelberg, October 2012, pp. 584–591.

[27] D. G. Lowe, "Object Recognition from Local Scale-Invariant Features," in *Computer Vision, 1999. The Proceedings of the Seventh IEEE International Conference on*, vol. 2. IEEE, September 1999, pp. 1150–1157.

[28] T. Joachims, "Making Large Scale SVM Learning Practical," *MIT-Press*, June 1999.

[29] A. Brost, N. Strobel, L. Yatziv, W. Gilson, B. Meyer, J. Hornegger, J. Lewin, and F. Wacker, "Geometric Accuracy of 3-D X-Ray Image-Based Localization from Two C-Arm Views," in *Workshop on Geometric Accuracy In Image Guided Interventions - Medical Image Computing and Computer Assisted Interventions 2009*. London UK: MICCAI, September 2009, pp. 12–19.

[30] Z. Zhang, "Determining the Epipolar Geometry and its Uncertainty: A Review," *International Journal of Computer Vision*, vol. 27, no. 2, pp. 161–195, March 1998.

[31] X. Armangué and J. Salvi, "Overall view regarding fundamental matrix estimation," *Image and Vision Computing*, vol. 21, no. 2, pp. 205–220, February 2003.

[32] A. Brost and et al., "Accuracy of X-Ray Image-Based 3-D Localization from Two C-Arm Views: A Comparison Between an Ideal System and a Real Device," in *Medical Imaging 2009, Visualization, Image-Guided Procedures, and Modeling*, M. I. Miga and K. H. Wong, Eds., February 2009.

[33] A. Rougee, C. Picard, Y. Trousset, and C. Ponchut, "Geometrical calibration for 3D X-ray imaging," in *Proceedings of SPIE Medical Imaging 1993: Image Capture, Formatting, and Display, Newport Beach, CA, USA, February 14–15*, Y. Kim, Ed., vol. 1897, February 1993, pp. 161–169.

[34] A. Brost, N. Strobel, L. Yatziv, W. Gilson, B. Meyer, J. Hornegger, J. Lewin, and F. Wacker, "Accuracy of X-Ray Image-Based 3D Localization from Two C-Arm Views: A Comparison Between an Ideal System and a Real Device," in *SPIE Medical Imaging*. International Society for Optics and Photonics, March 2009, pp. 72 611Z–72 611Z.

[35] A. Brost, F. Bourier, A. Kleinoeder, J. Raab, M. Koch, M. Stamminger, J. Hornegger, N. Strobel, and K. Kurzidim, "AFiT - Atrial Fibrillation Ablation Planning Tool," in *VMV*, E. E. A. F. C. Graphics, Ed., October 2011, pp. 223–230.

[36] A. Kleinoeder, A. Brost, F. Bourier, M. Koch, K. Kurzidim, J. Hornegger, and N. Strobel, "Cryo-Balloon Catheter Position Planning using AFiT," in *Proceedings of SPIE Medical Imaging 2012: Image-Guided Procedures, Robotic Interventions, and Modeling*, D. R. H. III and K. H. Wong, Eds., vol. 8316, February 2012.

[37] T. Kurzendorfer, A. Brost, F. Bourier, M. Koch, K. Kurzidim, J. Hornegger, and N. Strobel, "Cryo-Balloon Catheter Tracking in Atrial Fibrillation Ablation Procedures," in *Bildverarbeitung für die Medizin (BVM 2012), Berlin, Germany, March 18–20*, March 2012, pp. 386–391.

[38] F. Bourier, A. Brost, A. Kleinoeder, T. Kurzendorfer, M. Koch, A. Kiraly, H.-J. Schneider, J. Hornegger, N. Strobel, and K. Kurzidim, "Navigation for Fluoroscopy-Guided Cryo-Balloon Ablation Procedures of Atrial Fibrillation," in *Proceedings of SPIE Medical Imaging 2012: Image-Guided Procedures, Robotic Interventions, and Modeling*, S. M. Imaging, Ed., vol. 8316, February 2012.

[39] C. Kowalewski, F. Heissenhuber, D. Vukajlovic, N. Strobel, F. Bourier, T. Kurzendorfer, A. Kiraly, W. Wu, A. Kleinöder, A. Brost, M. Hoffmann, and K. Kurzidim, "Evaluation of the First Software Tool Featuring 3D Visualization of Cryo-balloon Ablation Catheters in Atrial Fibrillation Procedures," in *36th Annual Scientific Meeting*, HRS, Ed., May 2015, pp. 04–03.